Astronomy
&
Astrophysics

Structure and star formation in disk galaxies

II. Optical imaging[*]

J. H. Knapen[1], S. Stedman[1], D. M. Bramich[2], S. L. Folkes[1], and T. R. Bradley[1]

[1] Centre for Astrophysics Research, University of Hertfordshire, Hatfield, Herts AL10 9AB, UK
  e-mail: j.knapen@star.herts.ac.uk
[2] School of Physics and Astronomy, University of St. Andrews, Scotland KY16 9SS, UK

Abstract. We present optical observations of a sample of 57 spiral galaxies and describe the procedures followed to reduce the data. We have obtained images in the optical B and I broad bands, as well as in Hα, with moderate spatial resolution and across wide enough fields to image the complete disks of the galaxies. In addition, we observed 55 of our sample galaxies in the R and eight in the V band, and imaged a subset through a dedicated narrow continuum filter for the Hα line. We describe the data reduction procedures we developed in the course of this work to register, combine and photometrically calibrate each set of images for an individual galaxy. We describe in some detail the procedure used to subtract the continuum emission from our Hα images. In companion papers, we describe near-infrared imaging of the galaxy sample, and present analyses of disk scale lengths, and of properties of bars, rings, and H II regions in the sample galaxies. The images described here are available for use by other researchers.

Key words. galaxies: spiral – galaxies: structure – methods: data analysis – techniques: image processing

1. Introduction

The structure of disk galaxies has been studied in a quantitative way for decades now (e.g., de Vaucouleurs 1948; Freeman 1970) and although the field has much advanced since the early days of photographic plates, several old problems have not yet been solved, and new problems have appeared. Among the most important of such problems are the nature of the exponential disk, the evolution of bulges, the origin of spiral structure and its influence on star formation, the life cycle of bars, and the origin and influence of dark matter. Imaging of disk galaxies has evolved from the early days, when Hubble (e.g., 1926) used the largest telescopes available at the time to photograph galaxies, to fully automated all-sky surveys in the near-IR (e.g., 2MASS: Jarrett et al. 2003).

In planning the programme of which the results described here form part, we identified the need for a technically uniform set of images covering the complete disks of a well-defined sample of spiral galaxies. One of the main aims of this overall programme is the study of the distribution of scale lengths in different classes of spiral galaxies, and specifically to study possible differences between arm and interarm regions. This drove us to develop a significant imaging programme,

of near-IR K_s-band imaging on the one hand (described by Knapen et al. 2003, hereafter Paper I), and more conventional optical broad- and Hα narrow-band imaging on the other (this paper). Our sample consists of 57 nearby and not highly inclined spiral galaxies of all types, and since it contains a large number of galaxies which continue to attract significant attention from researchers (e.g., M 74, M 77, M 95, M 100) the importance of the currently presented set of images, along with those of Paper I, goes beyond our immediate research aims, which will be explored in a number of subsequent papers. The combination of these factors justifies the current publication of the details of the data collection and reduction. Workers in the field are welcome to peruse our images, through the CDS, and/or reduction scripts.

After briefly summarising the sample selection in Sect. 2 of this paper, we describe the observations and the reduction of the data in Sects. 3 and 4, respectively. The description of the final data set, in Sect. 5, is followed by a short concluding section (Sect. 6).

2. Sample

The selection criteria for the sample observed, as well as some of its statistical properties, have been described in detail in Paper I, and we only summarise the main points here. We selected all galaxies which are larger than 4.2 arcmin in

---

[*] FITS images are available in electronic form at the CDS via anonymous ftp to cdsarc.u-strasbg.fr (130.79.128.5) or via http://cdsweb.u-strasbg.fr/cgi-bin/qcat?J/A+A/426/1135

diameter, of spiral type, inclined less than 50°, and visible from the Northern hemisphere ($\delta > -20°$). The resulting sample contains spiral galaxies of all morphological spiral types, with and without bars, with and without nuclear activity of Seyfert, LINER, or starburst type, and of all spiral arm classes (cf. Elmegreen & Elmegreen 1987). All sample galaxies are relatively nearby, with an upper limit in systemic velocity of close to 2500 km s^{-1}. Apart from the optical observations described in the present paper, we also obtained images of all sample galaxies in the near-IR K_s-band. As described in Paper I, the latter images cover the complete disk of the galaxy in most cases, and most of the disk for all galaxies, and are almost all of sub-arcsec spatial resolution.

3. Observations

We present a complete set of images in the broad Harris B and I bands and in the narrow Hα band of our sample of 57 galaxies, and in addition R-band images of 55 of our 57 sample galaxies. Most of these images were obtained on the 1-m Jacobus Kapteyn Telescope (JKT) on La Palma, during a number of observing runs from 1999–2003. We also obtained images from the JKT through the service programme, where observatory staff performed the observations. A number of images, especially of the larger galaxies in our sample, were obtained with the 2.5-m Isaac Newton Telescope (INT) on La Palma (B: NGC 628, NGC 1073, NGC 3368, NGC 4254, NGC 4321, NGC 4395, NGC 4535, NGC 4725, NGC 4736; R: NGC 4321, NGC 5248; I: NGC 628, NGC 4321, NGC 4395, NGC 4535, NGC 4725, NGC 4736, 5457; Hα: NGC 4314, NGC 4395, NGC 5457). In addition to these new observations, we also made extensive use of the Isaac Newton Group (ING) data archive. After discarding a significant fraction of the images we originally found in the archive, about 15% of our final images were obtained from there. Reasons for discarding images, and repeating the observations, range from too old observations with too small a field of view (FOV), to lack of documentation on, e.g., the filters used. For NGC 3631 and NGC 4321, we used Hα images from the literature (see Sect. 4.4), while the broad-band images of NGC 4321 date back to Knapen et al. (1993a). The R-band image of NGC 5248 has been described in detail by Jogee et al. (2002).

A considerable variety of cameras and CCD detectors was used, but the principal ones were the camera on the JKT, imaging onto a SITe2 CCD with 2048 × 2048 pixels of a projected size of 0.331 arcsec each, and the wide field camera (WFC) on the INT. The latter has four EEV CCDs of 2048 × 4096 pixels, also with a projected pixel size of 0.331 arcsec. The unvignetted FOV of the JKT camera is ~10 arcmin, that of each of the four WFC CCDs is 11 × 22 arcmin. We used a set of Hα filters with central wavelengths matched to the recession velocities of the galaxies, and width in most cases around 50 Å, as listed in Table 1. Seeing conditions varied during the course of our observational campaigns and the seeing as measured from the final images ranges from 0.8 to 3.7 arcsec, with a median of 1.64, 1.39, 1.45 and 1.53 arcsec *FWHM* for the B, R, I and Hα images, respectively. Seeing values for the individual images are listed in Table 1.

All observations were accompanied by a sufficient number of bias and dusk or dawn sky flat fields for calibration (lack of such exposures was one possible reason for discarding archive images). On photometric nights, a number of Landolt (1992) standard stars and spectrophotometric standards were observed in order to provide the necessary photometric zero points (see Sect. 4.5).

4. Data reduction

The main problem we faced during the reduction of the large amounts of data we collected was the combination of images taken on different nights, under different conditions, and often with different cameras, pixel sizes, FOV, or orientation of the images on the sky. To manage this problem, we wrote a set of scripts in IRAF[1], aimed to handle the complete data reduction, including bias subtraction, flatfielding, and sky subtraction. We use a combination of IDL and IRAF scripts to subtract a scaled continuum from the Hα images. Each interactive script handles a specific aspect of the data reduction pipeline providing the advantages of increased efficiency and data quality control at each step without committing to the whole data reduction process in one go. We will describe some of these scripts in more detail below, but give a complete list with short descriptions here.

- `bias.cl` – Calculate the mean bias level as a constant from a set of bias frames.
- `flat.cl` – Create a mean flat field frame from a set of flat field frames and using a constant as the bias level.
- `reduce.cl` – Subtract the bias level as a constant from a set of science frames and flat field them all using a specified flat field frame.
- `meanimcombine.cl` – Combine a set of images of one object in a single waveband by averaging the images weighted by their exposure times, and performing the required scaling, rotation, and translation. The output image is scaled to an exposure time of one second and an option exists to align it to a Digitized Sky Survey (DSS) image.
- `medianimcombine.cl` – As `meanimcombine.cl` but using the weighted median rather than the weighted mean of the input images.
- `background.cl` – Subtract a constant sky background level from the image after determining the correct value by iteratively averaging and 3 sigma clipping across a user-defined area of background.
- `lineup.cl` – Lines up images of the same galaxy in different wavebands, scaling the images and changing their canvas size so that no data are lost in the process.
- `aminusb.cl` – Creates an $A - B$ image which maps the colour differences across the image, in magnitudes. The output image is produced after smoothing the image with the best seeing to match the seeing of the other by convolving it with the required normalised 2D Gaussian function.

Table 1. Details of the images obtained for our sample galaxies: total on-source exposure time in minutes (Cols. 3–6); seeing in arcsec as measured on the reduced images (Cols. 7–10); filter used for the Hα line, where $\lambda/\Delta\lambda$ is the central wavelength and filter width, in Å (Col. 11) and continuum (Col. 12) imaging; scale factor used to subtract the continuum from Hα (Col. 13); and size of the final image set in arcmin (Col. 14). Where only one number is given the image is approximately square. Notes: [1] see Sect. 4.4; [2] B-band and Hα images are only 8.0 × 8.0 arcmin.

Galaxy		Exposure time (min.)				Seeing (arcsec)				Hα filter	Cont. filter	Scale	Image size
NGC	Messier	B	R	I	Hα	B	R	I	Hα	$\lambda/\Delta\lambda$		factor	(arcmin)
210		20	15	40	40	1.6	1.6	1.4	1.3	6594/44	6470/115	0.516	8.1
337A		50	10	30	60	1.9	1.4	1.3	1.3	6594/44	R	0.026	8.1
488		35	10	10	60	1.5	1.5	1.9	1.5	6607/50	R	0.031	8.1
628	74	36	30	20	40	1.4	1.8	1.2	1.0	6570/55	I	N/A	11.2 × 22.6[2]
864		35	30	35	120	1.6	1.1	1.6	1.4	6594/44	R	0.062	6.9
1042		20	10	25	90	1.4	1.7	1.4	1.5	6594/44	R	0.021	8.1
1068	77	35	10	30	40	2.4	2.2	1.4	2.0	6594/44	R	0.019	9.5
1073		20	15	10	60	3.7	1.2	1.3	1.4	6594/44	R	0.018	8.9
1169		30	15	20	60	1.4	1.2	1.2	1.8	6626/44	R	0.019	8.1
1179		20	10	20	80	2.1	2.2	1.8	1.9	6594/44	R	0.018	6.5
1300		30	–	30	40	2.7	–	2.3	1.6	6594/44	I	0.012	6.1
2775		15	15	10	100	1.4	1.8	1.4	1.9	6594/44	R	0.044	5.6
2805		15	15	20	120	1.3	1.4	1.1	1.7	6594/44	R	0.048	6.5
2985		45	15	10	60	1.8	1.4	1.8	1.8	6594/44	R	0.045	6.1
3184		30	12	40	80	1.7	1.7	1.4	1.7	6570/55	R	0.024	8.1
3227		60	15	20	80	1.9	1.4	1.7	1.2	6594/44	R	0.020	7.3
3344		15	15	10	20	1.2	1.4	1.4	1.1	6570/55	R	0.025	8.9
3351	95	30	30	10	60	1.7	1.9	1.6	1.6	6570/55	6470/115	0.500	6.5
3368	96	60	15	20	20	2.3	1.1	1.6	1.7	6594/44	R	0.054	9.3
3486		15	15	20	60	1.2	1.3	1.3	1.3	6570/55	R	0.057	6.05
3631		45	10	30	30	1.6	2.2	1.3	1.3	6589/15	6565/15	N/A[1]	5.6
3726		15	15	30	60	1.2	1.4	1.5	1.3	6570/44	R	0.023	6.5
3810		15	10	10	100	1.2	1.4	1.2	1.3	6594/44	6470/115	0.425	7.3
4030		30	15	10	60	1.7	1.6	1.8	1.5	6594/44	R	0.024	6.9
4051		30	10	20	60	1.4	1.7	1.4	1.5	6570/55	6470/115	0.436	7.7
4123		30	15	20	60	2.3	1.3	1.4	1.3	6594/44	R	0.020	7.7
4145		15	20	20	40	2.5	1.4	2.5	2.7	6594/44	R	0.025	6.1
4151		15	15	10	60	1.9	1.5	1.4	1.4	6594/44	R	0.022	6.9
4242		15	15	10	60	1.4	1.2	1.6	3.2	6570/55	R	0.050	8.7
4254	99	15	15	10	40	2.1	1.1	1.2	1.5	6626/44	R	0.055	10.2
4303	61	30	15	50	60	1.6	1.3	1.7	1.4	6594/44	R	0.042	8.5
4314		15	15	10	20	1.4	1.8	1.3	1.3	6594/44	R	0.240	7.8
4321	100	10	5	5	20	1.9	2.1	1.9	1.0	6601/15	6565/15, 6577/15	N/A[1]	10.1
4395		15	20	9	30	1.9	1.2	1.6	1.8	6568/95	R	0.660	11.4
4450		15	15	10	60	1.6	0.8	1.5	0.9	6607/50	R	0.025	6.5
4487		15	15	10	60	3.2	1.2	2.9	2.0	6594/44	R	0.047	6.2
4535		30	15	10	60	1.9	1.6	1.7	1.9	6594/44	R	0.042	9.9
4548	91	30	10	20	60	1.5	1.7	1.4	1.7	6594/44	6470/115	0.418	8.2
4579	58	30	15	20	60	1.6	1.1	1.8	1.6	6594/44	R	0.050	8.6
4618		15	15	10	60	1.5	0.8	1.5	1.3	6570/55	R	0.025	7.9
4689		45	15	10	60	1.9	0.8	1.5	1.8	6594/44	R	0.038	8.6
4725		30	15	10	40	2.2	1.2	2.1	2.3	6594/44	R	0.038	11.4
4736	94	10	27	9	60	1.9	1.3	2.2	1.4	6570/55	R	0.043	11.4
5247		15	15	10	60	2.6	2.3	2.4	2.3	6594/44	R	0.018	8.5
5248		15	30	10	60	2.2	1.3	2.0	1.4	6594/44	R	0.005	8.5
5334		15	15	30	60	1.6	1.4	2.3	1.8	6594/44	R	0.020	8.5
5371		15	15	10	60	1.4	1.1	1.2	1.3	6626/44	R	0.040	8.1
5457	101	15	15	9	60	3.0	1.3	2.3	2.4	6570/55	R	0.250	11.5 × 22.9[2]
5474		15	15	10	60	1.3	1.2	1.3	1.2	6570/55	R	0.047	8.4
5850		15	15	10	60	1.4	1.6	1.3	1.5	6626/44	R	0.019	8.5
5921		15	15	10	40	1.4	1.3	1.4	1.2	6594/44	R	0.088	8.5
5964		15	15	20	80	1.8	1.3	1.3	1.8	6594/44	R	0.048	8.5
6140		45	10	30	60	1.5	2.0	1.2	1.4	6594/44	I	0.020	7.9
6384		30	15	40	60	1.7	1.7	1.4	1.8	6594/44	R	0.040	8.1
6946		15	15	20	60	1.4	1.5	1.2	1.4	6570/55	R	0.045	11.5
7727		15	–	30	60	1.7	–	1.4	1.7	6594/44	6470/115	0.520	7.3
7741		15	10	30	80	1.6	1.4	1.5	1.5	6570/55	R	0.023	8.1

- `smooth.cl` – Smooths image with the best seeing to match the seeing of the other by convolving it with the required normalised 2D Gaussian function.
- `contsub.pro` – An IDL program that aids in determining the correct scaling factor for the continuum images for producing the continuum subtracted Hα maps by plotting the continuum counts versus the Hα counts for each pixel and measuring the gradient.

4.1. Bias subtraction and flat fielding

All bias and sky flat field frames were inspected for quality and those with very low or high (non-linear or saturated) counts, or with abnormal structure or read out noise, were removed. Since for all the CCDs used for this project the structure in the bias frames is negligible, we subtracted a constant bias level from all images. The SITe2 chip on the JKT has a typical bias level of ~625 ADU in the "quick" mode that was used, and a read out noise of ~5.3 ADU. With an average of nine bias frames taken per night, this leads to an uncertainty of ~2 ADU, or ~0.3%, in the bias level.

After checking the internal consistency of the flat field frames for each filter and each night, they were entered into the `flat.cl` script, which we used to create a normalised master flat, one per night per filter. Assuming typical numbers for bias level and gain, the uncertainty in a typical normalised master flat is of order of 0.35%.

We next used the script `reduce.cl` to bias-subtract and flat field all images taken through a certain filter in a certain night. After removing the outer areas of the chip, the reduced science frames are passed once through the cosmicrays task in IRAF to remove in an automated way the majority of hot pixel events.

4.2. Image combination

At this point in the data reduction procedure there is usually more than one image per filter per object. This is an advantage because if these images are of comparable quality they may be combined to produce an image with a greater signal to noise ratio. The images may be oriented differently, however, have a different FOV, and may have been obtained with different instruments, and under different conditions. After renaming the multiple individual images appropriately, they are entered into the script `meanimcombine.cl`, along with a DSS image if required. The script does the following:

1. Divide each image by its exposure time in seconds, as obtained from the header.
2. Ask the user to mark interactively three stars common to all the images (and two of these common to the DSS image).
3. Map each image onto the image with the smallest pixels (which is effectively the most detailed image) while preserving flux, and using parameters for geometric scaling, rotation and translation as determined from the fits to the star positions. This can lead to some loss of information if the FOV of the most detailed image is smaller than that of one or more of the other images, an effect that we prevent by manually copying the former image onto a larger pixel

grid. This script may also lead to blank areas on some images where data does not exist.
4. Combine the images by averaging the pixel values, weighted by the exposure times of the images, and ignoring blank pixels, to produce a combined output image. We have a second version of the script (`medianimcombine.cl`) which combines images by using the median value of the pixels, in the process removing most of the cosmic ray hits or otherwise bad pixels. This latter script is used only on images which are virtually identical, because for instance a different background or higher counts level in one of three images can lead to an unacceptable loss of information when median combination is used.
5. Using the two common stars marked in the DSS image, the script rotates the output image in order to line it up to the DSS image. This results in an output image where North is up, and East to the left, to an accuracy of better than 1°.

The combined output image has an effective exposure time of 1 s which is represented in its header by the keyword EXPTIME = 1. The image represents a total exposure time, however, equal to the sum of all the individual exposure times of the images used in the combination algorithm. We include this total exposure time, in minutes, in Table 1. At this point, there is only one image per filter per object.

4.3. Sky background subtraction and image registration

The script `background.cl` allows the user to mark interactively an area of approximately flat sky background, ideally far removed from the galaxy being imaged. Since this area may well include a couple of stars or cosmic rays, the script incorporates an interactive 3σ clip algorithm with a tolerance of 0.02% to derive the underlying background level. This level is then subtracted as a constant from the whole image. The method works well when the image has a flat background, and large areas without galaxy emission. It delivers merely an approximation, however, when the image has no areas free of galaxy emission, or when it shows a background with structure, e.g., due to non-perfect flat fielding. In these cases, the script `background.cl` was used to estimate the background level by running it on the flattest areas with the lowest counts available in the image.

To register the sets of images associated with a particular galaxy, all the images in that set (at least B, I, K_s, and Hα) are entered into the script `lineup.cl`. This script uses part of the functionality of the `meanimcombine.cl` script (see above), and again requires a common set of three stars to be marked in each image. The script identifies the image with the smallest pixels (i.e., the most detailed image) and re-grids all other images so these will have the same pixel scale as the most detailed image. The script then maps all images onto the image with the largest FOV, thus ensuring that no information is lost. Any areas in the images that lack data are marked as blank by setting these pixels to zero. This approach has a drawback which is that the size of the image files grows due to both smaller pixels and

larger areas. By compressing the images much can be gained though, because the areas on the outside of the images which are filled by pixels with value zero can be very effectively compressed. Flux is conserved throughout this procedure. Finally, the images are trimmed to a standard and usually square size.

4.4. Continuum subtraction from the Hα images

In order to subtract the continuum emission from our Hα images, two different techniques were used, depending on the origin and quality of the images and on the kind of continuum image available. For NGC 3631 and NGC 4321 we used Hα images obtained with the WHT, for which the continuum subtraction technique has been described in detail by Knapen et al. (1993b), with more specific details given by Rozas et al. (1996) for NGC 3631 and by Knapen (1998) for NGC 4321. As detailed in Table 1, for most of the remaining galaxies we used a broad-band *R* image, whereas for the others we used either an image obtained through a special Hα continuum filter with central wavelength 6470 Å and *FWHM* 110 Å (hereafter called 6470/110), or an *I*-band image.

Since at this stage in the reduction the images have been aligned, registered and background-subtracted, the one remaining parameter to be determined is the scaling factor, which determines how the continuum image must be scaled to match the intensity level of the continuum emission in the Hα line image. For each galaxy, we smoothed the image with the highest resolution to that of the other. We then used a combination of two techniques to derive the scaling factor. In the first, we basically follow the approach described by Böker et al. (1999). After re-binning, and after excluding a user-specified percentage of the brightest pixels (due to, e.g., foreground stars), we plot the intensity, in counts per second, of each pixel in the Hα image versus the intensity of the same pixel in the continuum image. As described by Böker et al. (1999), in the absence of line emission and in the case of constant colour across the field, the resulting relation should be a straight line, down to the noise level. Deviations from this straight line will be due to pixels which trace colour variations due to different stellar populations, differential extinction effects, Hα emission, or a combination of these. The plot will show most pixels in the image located along a narrow band, with the minority of pixels that trace Hα emission located above it (see Fig. 1 for an illustration). Points below the band are scarce because very few pixels will trace either excess continuum emission, or reduced line emission. Such points could have their origin in, for instance, Hα absorption in foreground stars, saturation in one of the two images, or sporadic events like cosmic rays. The slope of a line fitted to the continuum band will give the scaling factor, and the origin of the line will give an additional estimate of the background in both the line and continuum images (Fig. 1).

While in a number of well-defined cases (high-quality Hα images, and an accompanying continuum image taken through the 6470/115 or *R* filter) the slope of the line as described above gives a very good determination of the scaling factor for the continuum subtraction, we checked the result of this first method in all cases using a second method. Here,
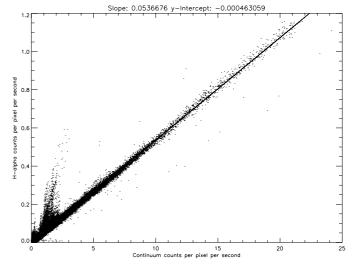

Fig. 1. Intensity, in units of counts per pixel per second, of each pixel in the Hα image of NGC 3368 versus the intensity of the same pixel in the continuum image, taken through the 6470/115 filter. Most points outline continuum-only emission, and the drawn line is a fit which gives an estimate of the scaling factor to be applied to the continuum image before subtracting it from the Hα image. A limited number of pixels traces Hα emission in the galaxy, and can be seen above the continuum band.

we measure the integrated intensity of a number of non-saturated foreground stars in the line and continuum images, and deduce the scaling factor from the average ratio of these intensities. Some stars have enhanced or depressed Hα emission, and in the absence of further information on the stars imaged we identified such stars by their deviant line/continuum intensity ratio. This problem was not severe because most of our Hα images were taken through Hα filters that were not sensitive to Hα emission at rest wavelength.

We found that the second method gave consistent results, both internally (different stars in the same image) and externally (in comparison to the pixel-to-pixel method described above). For example, in NGC 3368, the scaling factor determined using the first method of comparing the continuum and line counts at each pixel is 0.0537, whereas the second method, using the foreground stars in the image, gives a scaling factor of 0.0545. We used the foreground star method in all cases to check and constrain the scaling factor as derived from the pixel-to-pixel method. In those cases where the pixel-to-pixel method did not give conclusive results, a scaling factor as derived from the foreground stars was used.

The minimum number of foreground stars needed to obtain a reasonable constraint on the scaling factor was found to be six, a number which results in a typical error of around 5% in the scaling factor. With more stars available, and/or with further constraints from the pixel-to-pixel method, the uncertainty is even lower. Since the *R*-band covers the Hα line, the flux in the Hα image was corrected by about 3% whenever an *R* image was used as continuum (cf. James et al. 2004). To produce the continuum subtracted image, the continuum image was simply multiplied by the scaling factor, and the result subtracted from the line image. Scaling factors as used are listed in Table 1.

Identical filter combinations can give rather different scaling factors because the observing conditions are not always the same for both images. If, for instance, the continuum image is observed on a night with higher extinction (due to, e.g., thin clouds or to dust in the atmosphere), the scaling factor for that image will be higher than if the conditions would have been better.

We performed a number of specific tests to define the impact of the uncertainties introduced by the scaling factor on the luminosities of individual H II regions, especially when using the *I*-band filter. In both sets of tests, we compare integrated intensities of selected well-defined H II regions at different distances from the nucleus of a galaxy. Both changes in the scaling factor, and in the wavelength of the continuum image, will translate into smaller errors further out into the disk, where the level of continuum emission, as well as the effects of dust, will be reduced as compared to the central regions. In the first set of tests we compared H II region luminosities as measured from Hα images from which appropriately scaled 6470/115, *R*- and *I*-band images had been subtracted. We found that the 6470/115 and *R* continua lead to random errors in H II region luminosities that are less than 2%, without any systematic error. The 6470/115 and *I* continua lead to similar random errors, but also to a slight systematic difference of up to 5%. We find no evidence for an increase in this error with decreasing distance to the nucleus. In the second set of tests, we compared the integrated intensities of selected H II regions while changing the scaling factor within the range of uncertainty that accompanies our determination of that factor. Here we do find, not surprisingly, that uncertainties in the H II region luminosities are higher for those in the circumnuclear regions (at about 10–15% for the nucleus itself and the innermost H II regions, namely those within 0.5 kpc of the nucleus) than for those in the disk (at about 2–5%). We conclude from these tests that (1), although not ideal, it is certainly safe to use *I*-band images for continuum subtraction, (2), the best results are obtained by using either 6470/115 or *R*-band images, and (3), uncertainties in the continuum subtraction lead to uncertainties of a few percent at most in Hα luminosity and flux in the disks of our sample galaxies, although higher in the nuclei and circumnuclear regions, where they reach up to 10–15%.

4.5. Photometric calibration

Many of our images were either taken under non-photometric conditions, or (in the case of all images obtained from the archive) no guarantee could be found that conditions during the observations had in fact been photometric. We combined all good images, from photometric and non-photometric nights, and calibrated them once the final, combined, images had been produced. For this purpose, individual galaxy images, as well as standard star exposures, obtained during those of our own observing nights for which we could guarantee photometric conditions, were maintained separately throughout the reduction process. We used a number of photometric nights during our final observing runs to obtain short calibration images of those galaxies and in those filters where up to that moment we
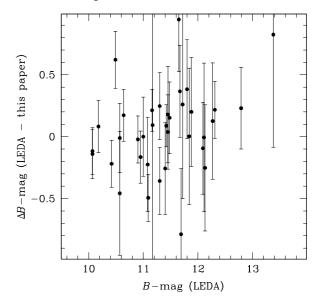

Fig. 2. Comparison between the total *B*-magnitudes for our sample galaxies as determined in this paper and as obtained from LEDA. The error bars indicate a combination of uncertainties as derived for our data and as given by LEDA, with the latter being the dominant source of uncertainty.

had no calibration. In the end all *B*, *I* and Hα images, and 44% of the *R*-band images, have been calibrated photometrically.

All photometric images were calibrated using the images of standard stars, mostly selected from Landolt's (1992) list for the broad band observations, and from a variety of sources for the narrow-band imaging (including Massey et al. 1988; Oke 1990). Following the same procedure as in Paper I, these calibrated but short images were then used to calibrate the images in the final data set. This was done by comparing the total flux in a certain area in the image to the flux as measured in exactly the same area in the other image. Normally, this area was circular and centred on the galaxy's nucleus, except where the nucleus was saturated in one of the images, in which case an annular area was used. In two galaxies, emission from foreground stars was used in addition to that from the galaxy itself. In all cases, differences between the two images, for instance in pixel size and background, were carefully taken into consideration.

The resulting photometric calibration was checked in a variety of ways against values published in the literature. For instance, we validated that radial profiles derived from our images compare favourably with the ones published by de Jong & van der Kruit (1994): differences are below 0.2 mag in the three galaxies which occur in both samples. We also considered differences between the total magnitudes derived from our imaging and those collected in the Lyon-Meudon extragalactic database (LEDA). The results, shown in Fig. 2, are similar to those reported by de Jong & van der Kruit (1994, their Fig. 6), who compared total magnitudes as found by them and as published in the RC3 (de Vaucouleurs et al. 1991). As in their case, we find a large scatter, but crucially around a value of zero in the magnitude difference. The scatter is due to a variety of reasons, such as the data points compiled in LEDA, the difficulties in determining total magnitudes from our data in cases where

the imaged area of sky is not much larger than the galaxy, or our own calibration. Overall, we are confident of the photometric calibration of our images, without claiming high-precision photometry.

5. Description of the final data set

The final data set for each of our 57 sample galaxies consists of images in the broad B and I bands, as well as in Hα. In addition, K_s images were obtained for all galaxies, as described in detail in Paper I. For all except two galaxies (NGC 1300 and NGC 7727), R-band images were obtained, and in some cases (NGC 628, NGC 3184, NGC 3351, NGC 3631, NGC 4321, NGC 4395, NGC 5371, and NGC 5457) we obtained also a V-band image. All images were reduced to equivalent exposure times of 1 s, and were placed on the same pixel grid for each galaxy. This latter step implies that all images in the final data set have pixels of 0.241 arcsec squared (the smallest pixel size used, namely that of the near-IR INGRID camera, see Paper I), and that all images of any given galaxy are exactly aligned to each other, are correctly oriented (to within the accuracy dictated by the DSS images), and are of the same size. For each galaxy, we also produced a continuum-subtracted Hα image.

We updated the headers of the FITS image files to include a description of the world coordinate system. For this, we used the position of the galaxy as given on the NASA-IPAC Extragalactic Database, NED, and tied this in with the centre position on our images. We also included a keyword in the header of each image giving the calibration constant which can be used to derive surface brightnesses and magnitudes from the images. The images described in this paper are available for general use through the CDS.

6. Conclusions

We present an extensive set of optical broad- (B, R, and I) and narrow-band (Hα) images of a sample of 57 Northern, not highly inclined, spiral galaxies of all types. The images were obtained partly from the literature and from the ING data archive, but mostly from our own observations with the 1 m JKT and the 2.5 m INT on La Palma. In this paper, we describe the observations and the data reduction procedures. Because of the characteristics of the data set, obtained over the years with different instrumentation, we developed a set of IRAF scripts, described in detail here, which allow us to handle the volume of data involved in this project. We also describe in some detail the procedures followed to subtract the continuum from our Hα emission line images, and estimate uncertainties associated with the continuum subtraction. For each of our 57 galaxies, our final data set consists of aligned images in the B, I and K_s (from Paper I) broad bands, as well as in Hα. For 55 of these

galaxies, the set also contains an R-band image, while a V-band image is available for eight galaxies.

We will use the image set in subsequent papers to investigate the distribution and properties of the H II regions in the disks and central regions of the galaxies, the properties of their bars and central regions, and the mutual influence of star formation and spiral arms. The images described in this paper will be made available for general use through the CDS.

References

Böker, T., Calzetti, D., Sparks, W., et al. 1999, ApJS, 124, 95
de Jong, R. S., & van der Kruit, P. C. 1994, A&AS, 106, 451
de Vaucouleurs, G. 1948, AnAp, 11, 247
de Vaucouleurs, G., de Vaucouleurs, A., Corwin, J. R., et al. 1991, Third reference catalogue of Bright galaxies (New York: Springer-Verlag) (RC3)
Elmegreen, D. M., & Elmegreen, B. G. 1987, ApJ, 314, 3
Freeman, K. C. 1970, ApJ, 160, 811
Hubble, E. P. 1926, ApJ, 64, 321
James, P. A., Shane, N. S., Beckman, J. E., et al. 2004, A&A, 414, 23
Jarrett, T. H., Chester, T., Cutri, R., Schneider, S. E., & Huchra, J. P. 2003, AJ, 125, 525
Jogee, S., Knapen, J. H., Laine, S., et al. 2002, ApJ, 570, L55
Knapen, J. H. 1998, MNRAS, 297, 255
Knapen, J. H., Cepa, J., Beckman, J. E., Soledad del Rio, M., & Pedlar, A. 1993a, ApJ, 416, 563
Knapen, J. H., Arnth-Jensen, N., Cepa, J., & Beckman, J. E. 1993b, AJ, 106, 56
Knapen, J. H., de Jong, R. S., Stedman, S., & Bramich, D. M. 2003, MNRAS, 344, 527 (Erratum MNRAS, 346, 333; Paper I)
Landolt, A. U. 1992, AJ, 104, 340
Massey, P., Strobel, K., Barnes, J. V., & Anderson, E. 1988, ApJ, 328, 315
Oke, J. B. 1990, AJ, 99, 1621
Rozas, M., Beckman, J. E., & Knapen J. H. 1996, A&A, 307, 735